Drag and Heat Flux Reduction using Counterflow Jet and Spike - Analysis of their Equivalence for a Blunt Cone Geometry at Mach 8

B. John[†], D. Bhargava, S. Punia and P. Rastogi

School of Mechanical Engineering, Vellore Institute of Technology, Vellore, Tamil Nadu, 632014, India

† *Corresponding Author Email*: *bibinjohnm@gmail.com*

ABSTRACT

This study aims to explore equivalence between active and passive flow control techniques in reducing the wave drag and surface heat flux over a blunt cone model kept in Mach 8 stream. Computational investigations were carried out by using finite volume-based compressible flow solver. Throughout the study, the solution of governing equations is sought by assuming two dimensional-axisymmetric nature of the flowfield. Both counter flow-stagnation point injection and forward facing-physical spike are considered to mitigate the excess drag and heat flux experienced by a blunt body representing the nose cone section of a hypersonic vehicle. Eventually, based on identified drag reductions, the present study proposes equivalence cases between these two methods. It is shown that a pointed spike of L/D=1 provides almost the same drag reduction as the counterflow injection jet with a pressure ratio of 8.25. Similarly, other equivalence cases are identified and the physics behind them is explored. The identified equivalence is expected to help the designers in effectively replacing one technique with another according to the requirement. Equivalence matrix is presented for different spike cases in terms of injection ratios of counterflow injection.

Keywords: Counterflow injection; Physical spike; Blunt body; Hypersonic; Drag reduction; Aerodynamic drag, Shock interaction, Recirculation region.

NOMENCLATURE

C_d	coefficient of drag	P_{0j}	total jet pressure
C_p	coefficient of pressure	R	nose radius of the blunt body
D	base diameter of the blunt body	S	curve length of the blunt body from stagnation point
L	spike Length		
M	Mach number	St	Stanton number
P_∞	free stream static pressure	T	temperature
		X	horizontal distance
P_{01}	free stream total pressure ahead of the shock	Y	vertical distance
P_{02}	free stream total pressure behind the shock		
P	local static pressure	ρ	density
PR	pressure ratio	μ	molecular viscosity

1. INTRODUCTION

With the rapid development of aerospace technologies, hypersonic vehicles, once a quixotic dream, are now being developed more readily, and have become the cynosure of high-speed travel.

Hypersonic speed ranges from Mach 5 to Mach 25. However, this classification isn't a hard and fast one. The flow doesn't turn into hypersonic instantly at Mach 5, rather the different physical phenomenon involved in hypersonic flow regime become more important progressively as the Mach number increases. Some of them may become distinctive

even below the hypersonic range, such as Mach 3, whereas some might only become significant only above Mach 7 (Anderson Jr 2006).

Hypersonic aerodynamics and its underlying mechanisms are unlike the conventional supersonic aerodynamics. Generally, measures are taken to prevent separation of flow, but in the case of hypersonic speeds, purposely flow separation is made to happen ahead of the stagnation region of space change vehicle's stopchange nose-cone section. This alleviates two of the most critical problems associated with hypersonic speeds-enormous drag and heat flux (Bogdonoff 1959). In the hypersonic speed range, pressure drag is dominant over the skin friction drag because of the formation of shock waves. Massive drag occurs as the fast-moving vehicle compresses the air in front of it, slamming into the air particles faster than the particles can get out of the way. Further, this also creates high-temperature zones in the vicinity of the space vehicle's surface, thus elevates the surface heat flux. A vehicle designed to fly at hypersonic speeds must be able to withstand this intense heat generated due to air friction and shock waves. Thus, to decrease this heat, the nose of the vehicle is made blunt which avoids any thin shock layers to be present close to the vehicle body and results in a highly curved detached bow shock at a certain distance ahead of the nose (Allen and Eggers Jr 1958). However, this bluntness engenders an issue of increased drag, which results in the concomitant issue of increased fuel consumption. The lesser the drag is, the less would be requirement of fuel expended to overcome the drag forces. Consequently, payload volume can be increased for the same. Therefore, vehicle aerodynamics for decreased drag force and reduction of heat flux become critical parameters that govern the design of such vehicles. Considering these facts, many researchers have studied the aerodynamics of the flow over a blunt body and have devised several methods such as solid spikes, energy deposition, counterflow injection of coolant gas from the stagnation point, etc., to reduce drag and heat flux.

2. LITERATURE SURVEY

2.1 Physical Spike Based Drag Reduction

This method is an efficacious passive means of drag reduction. It employs a spike protruding from the body's stagnation point. The spike diverts a significant portion of the flow away from the body and alters the bow shock to a conical (oblique) shock, completely changing the flowfield pattern. Various experimental investigations and numerical simulations were carried out in the past few decades with a variety of objectives. The typical parameters considered in these studies were Mach number, Reynolds number and different length and geometries of the spike. Crawford in 1959 (Crawford 1959) experimentally discerned the effect of spikes with different L/D ratio (Spike length / Nose diameter of blunt body) on flowfields associated with

hemisphere-cylinder at a freestream of Mach 6.8 by varying the Reynolds number of the flow. The investigation yielded that increasing the spike length reduced the drag, but only up to a threshold maximum value of L/D ratio. Increasing the spike length further caused an increase in drag coefficient. The investigation also showed that heat transfer rate was immensely affected by the type of flow over the separated boundary layer. For flow with high Reynolds number, spike increased the heat transfer rate whereas for low Reynolds number flow, it decreased the heat transfer rate.

In 1962, Wood (Wood 1962) through an experimental investigation came to the conclusion that the flow close to the point of reattachment on the blunt body essentially governs the size and the physical shape of a region of the separated flow. Later in 1995, Yamauchi *et al.* (1995) explored the variations in flowfield over a blunted body with a protruding spike at different Mach numbers (2.01, 4.15 and 6.80) with varying L/D ratio and gave conclusions which were in agreement with previously published studies. The spike length had a pronounced effect on drag, and the flow in the separated region wasn't significantly influenced by the freestream Mach number. Mehta (2013) numerically studied the effect of a physical spike (L/D=0.5) in reducing the pressure drag and heat flux for a free stream of Mach 6 at zero angle of incidence and concluded that hemispherical disc spike gave high drag in comparison to the flat-faced disc spike.

In 2010, Kalimuthu *et al.* (2010) evaluated the aerodynamic characteristics without spike and after attaching a spike (L/D = 1.5 and 2) to a hemispherical blunt nosed body at Mach 6 while simultaneously varying the AOA (angle of attack) ranging from 0 - 8 degrees, with a step of 1 deg . It was found that both drag and lift coefficient increased with the angle of attack for both with and without spike cases. Again in 2019, Kalimuthu *et al.* (2019) assessed aerodynamic characteristics - drag coefficient, lift and pitching moment, associated with five different types of spikes, namely, conical aerospike, hemisphere aerospike, flat-faced aerospike, hemisphere aerodisk and flat-faced aerodisk (L/D ratio of 0.5, 1, 1.5 and 2) attached to a blunt nose body at Mach 6.0, and angle of attack up to 8 degrees. This investigation showed that the drag and pitching moment coefficient decreased whereas the lift coefficient increased as the L/D ratio and angle of attack increased.

Gerdroodbary and Hosseinalipour (2010) studied the effects of the reattachment point on reducing the surface convective heat flux for four types of spikes (with varying L/D ratio), viz. cut, sharp, flat-aerodisk \& hemispherical aerodisk for different angle of attack (3, 7, 10 and 12) at a nominal Mach 5.75 freestream and recommended that low L/D spike should be avoided as it leads to the impingement of reattachment shock and bow shock at the same location. Sahoo *et al.* (2016) investigated three different types of spikes, viz. sharp, blunt and

aerospike on a hemispherical blunt body for the freestream flow of Mach 2. The sharp spike lead to a 30\% reduction in drag whereas the aerospike and the blunt spike for the same length lead to a reduction of about 45\%. Others have also made an important observation that as the spike length is increased, pressure fluctuations also increased. In general, blunt and aerospike exhibited fewer fluctuations than the sharp spike.

2.2   Counterflow Drag Reduction Method

It employs injection of an opposing jet from the stagnation point of a blunt body that changes the distribution of temperature and pressure over the configuration. All these aerodynamic characteristics are evaluated for different injection pressure ratios, $PR = P_{0j} / P_{02}$. Warren in 1960, through an experimental investigation of ejecting helium and nitrogen coolant gases from the stagnation point of a bluff body at Mach 5.8 freestream, discerned that a straight-out ejection was an efficacious method to decrease heat flux on the body surface (Warren 1960). In 1966, Finley (1966) using an analytical model of counterflow jet ejection from an orifice at the nose of the body, found the dependency of aerodynamic characteristics on the Mach number of the opposing jet and its flow-force coefficient. The study proved the importance of a critical range of total pressure ratio (P_{crit}) below this critical range the flow is generally marked as unsteady. The critical range pressure is a function of nose shape and jet size. Finley also classified the flowfield around a blunt body with counterflow jet into steady, unsteady and the transitional zone - similar to as observed in the case of spike by Feszty *et al.* (2004) and Panaras and Drikakis (2009).

Venukumar *et al.* (2006), experimentally investigated the flow features around a large angle blunt cone incorporated with counterflow jet kept at Mach 8 and reported a 30-45\% reduction in coefficient of drag for different jet pressures. In 2008, Kulkarni and Reddy (2008) investigated the potential of counterflow supersonic jet in reducing the drag over a 60^0 apex angle blunt cone put inside a hypersonic freestream at Mach 8 and reported that the drag reduction increased with increasing stagnation enthalpy. For a particular pressure ratio, with an increase in the flow enthalpy by a factor of 2.5, the percentage of drag reduction increased by a factor 2

In 2013, Yisheng (2013) numerically studied drag reduction by the counterflow jet in a supersonic freestream and found the results to be in agreement with validated studies. Yisheng introduced a new parameter R_{PA} combining the flux with total pressure ratio.

$$R_{PA} = \frac{P_{0j}A_j}{P_{0\infty}A} = \frac{P_{0j}R_j^2}{P_{0\infty}R^2}$$

This new parameter represented the intensity of the opposing jet. The study also reported that the same drag coefficient and the shock wave position could be obtained for the same R_{PA} with different total pressure ratios and different fluxes change. Zhou *et al.* (2013) studied extensively about the LPM and SPM mode of jet. It was noticed that below P_{crit} the LPM mode is exhibited and is characterized by mild under expanded flow which undergoes regular reflections. Whereas for a pressure ratio greater than P_{crit} a largely under expanded flow is noticed which is the SPM mode. It has been known that the maximum overall drag reduction is noticed in LPM regime which has a greater shock stand off distance than SPM. However, LPM causes an increase in peak pressure and heat flux at the reattachment point which contributes to its drawback.

Deng *et al.* (2018) studied the effect of Aerospike and Counterflow jet in reducing the drag and heat flux and special attention was given in studying the LPM mode of the jet. It was found out that for a hypersonic freestream of Mach 8, counterflow jet provided better reduction in peak pressure and high-pressure areas at high angles of attack. The jet was able to sustain its flow structure in terms of shock dispersion and jet penetration even at higher angle of attack. Where a spike effectiveness was seen to decrease with increasing angle of attack. It was also noticed that in case of LPM counterflow jet a considerable increase in shock standoff distance was noticed along with the strong flow unsteadiness. Zhang *et al.* (2018) conducted a study for different sinusoidal pulsed jets with time periods ranging from T =0.5 ms to T =2.0 ms and found out that although the pulsed jets are effective in reducing the heat flux against the steady counterflow jet, they offer lesser drag reduction. A better drag and heat flux reduction was seen for the counterflow jet with a larger period. Recently, Li *et al.* (2020) conducted a study where the conventional solitary counterflow jet was replaced by a complex mechanism of four jets placed uniformly around the geometrical body. It was observed that the flowfield has significant changes due to the interaction of adjacent holes along the lateral direction. Consequently, four recirculation regions were formed which were seen to be extremely beneficial for reducing drag as well as providing thermal protection during hypersonic flights.

3.   Necessity of Equivalence

At hypersonic speeds, especially in the case of re-entry vehicles, most of the past studies proved the incapabilities of the physical spike. Although physical spike offers significant drag reduction at zero angle of attack (AOA), the spike tip is subjected to extremely high temperature, which ultimately would lead to its rupture. At AOA's other than zero, using a spike might makes the flowfield entirely unstable. Furthermore, the spike method, being a passive means to drag reduction offers no in-flight

real-time maneuvering. In light of these issues, the counter-flow jet method, although expensive and complex to implement, proves to be more effective and practical. It allows in-flight maneuvering with a significant reduction in drag and considerably more reduction in the case of heat flux on the body surface. Most of the past research studies are based only on the development of these two techniques. This study aims to expound upon obtaining an equivalence between them by specifying certain cases with the same drag. It also incorporates heat flux analysis to discern the effectiveness of these methods in reducing the heat conducted within. These equivalence cases can be employed when there is a need to switch from a physical spike to counterflow jet and vice versa, based on the application's requirement.

4. METHODOLOGY

4.1 Governing Equations

The flowfield over the blunt body is resolved by numerically solving the two-dimensional axisymmetric compressible Reynolds-Averaged Navier stokes (RANS) equations using finite volume solver (ANSYS 18.0). The flow governing equation for this case includes continuity, momentum and energy equations. Since the flow is assumed as 2D-axisymmetric one, the momentum equation in the angular direction is not solved explicitly. Instead, suitable source terms are included in the axial and radial momentum equations transformed to cartesian coordinate system. Therefore, four governing equations are solved to find five unknowns (pressure, u-velocity, v-velocity, temperature and density) of the mean flow. Since the unknown variables are more than the number of equations, one has to consider an additional relation to correlate pressure and density. The present study considers the working fluid (air) as ideal gas, hence ideal gas equation is used here to ensure closeness of the solution.

As the flowfield is turbulent in nature additional equations are essential to capture the turbulent characteristics of the flowfield and to derive the mean flow parameters. In this study, $k - \omega$ SST (Menter 1994) turbulence model is employed to meet this purpose. $k - \omega$ SST combines the best of the $k - \epsilon$ model and the $k - \omega$ model, activating either one according to the key aspects of the flowfield. The SST formulation, therefore shifts to $k - \epsilon$ when far from the boundary/wall region. Whereas, the combination of the SST formulation with $k - \omega$ helps in accounting for the turbulent shear stress transportation and provides an accurate prediction of the amount of flow separation as well as its onset under adverse pressure gradients. This transformation is taken care of by an extra term of cross diffusion defined as, A well tested upwind scheme (AUSM) is employed for the calculation of convective fluxes at the faces of the computational

domain. A cell centered Green-Gauss approach is employed to calculate gradients at the cell centroids. Later the essential gradients of the flow properties are evaluated at the faces and computed for the viscous fluxes over there. The net fluxes integrated over the entire faces of the cell later used to compute the updated convective vector during implicit time marching. Second order accuracy in spatial discretization is followed to ensure higher order accuracy of the solution. Solution iterations are continued till the reach of convergence criteria.

4.2 Geometry

The blunt cone geometry of 60^0 apex angle and a bluntness ratio of 0.857 with 70 mm base diameter is used\change. At the nose tip of the blunt cone geometry, a 2 mm hole is provided for sonic air jet injection. The geometry employed for the present study is adapted from the experimental study of Venukumar and Reddy (2007). The design of spikes, viz. pointed and blunt are same as those used by Sahoo *et al.* (2016) in his investigations with spike diameter of 0.133D. Previously, Gerdroodbary *et al.* have stated that 2D-axisymmetric simulations are capable of accurately predicting the flowfield and surface properties under similar flow conditions. (Gerdroodbary and Hosseinalipour 2010). Therefore, due to the symmetry of the body about its axis of rotation and the consideration of zero angle of attack of the flow, 2D-axisymmetric simulation is used instead of complete 3D simulation which reduced the computational time greatly.

5. VALIDATION OF SOLUTION METHODOLOGY

5.1 Computational Grid and Boundary Conditions

As mentioned in the previous section, a two dimensional computational domain is employed for the present study. The computational domain is further meshed using quadrilateral, non-overlapping control volumes. In order to capture the turbulence and the viscous effects near the wall, an adequate grid clustering is employed there. The boundary layer meshing strategy followed near the wall region ensures y^+ requirement of two equation-turbulence model used in the present simulation. In addition to near wall clustering, grid refinement is done for the region upstream of the stagnation point of the blunt body to ensure accurate capturing of counterflow jet and its close interaction with the standing bow shock. Figure 1 shows the grid used for the study and the applied boundary conditions. The hypersonic inlet of the computational domain is assigned with freestream flow properties. The freestream conditions employed for the current study consist of freestream Mach number of 8.0, static pressure of

219.2Pa and static temperature of 172.4K. The wall boundary is specified as isothermal with no-slip and is set with constant temperature of 300K. For the non-injection case the entire inner curved surface is taken as wall, whereas for the injection case a hole of 1mm radius is provided at the stagnation region of the blunt body. The injection boundary is specified as pressure inlet and is set with specific injection pressure. The outlet of the domain is expected to be predominantly supersonic, hence outlet parameters are extrapolated from the immediate interior cells.

Table 1 Grid size and Maximum Y+ for Different Grids

Grid	Size	Max Y+
Coarse	250 x 230	7.5
Medium	400 x 280	2
Fine	520 x 420	0.7
Extra Fine	650 x 580	0.4

Table 1 shows the maximum $Y+$ for different grids. Data presented in Fig.2 is the evidence that the first two levels of grids are not accurate enough to proceed with. However, the third level (fine) is sufficient enough to predict the flowfield with decent accuracy. Hence the results obtained with the fine grid are used for further discussions. It is to be noted here that only the steady state results obtained on different levels of the grid are employed here to demonstrate the grid independence nature of the solution. The residuals of mass, momentum and energy are considered to monitor the convergence of the solution. Figure 3 shows the convergence history of the residuals, where it can be seen that the residual of continuity starts to oscillating around 10^{-5}. Thus, additional time dependent variation in drag coefficient is examined to ensure the convergence. The drag variation trend is noted to be converging to a constant value as the flowfield attains steady state.
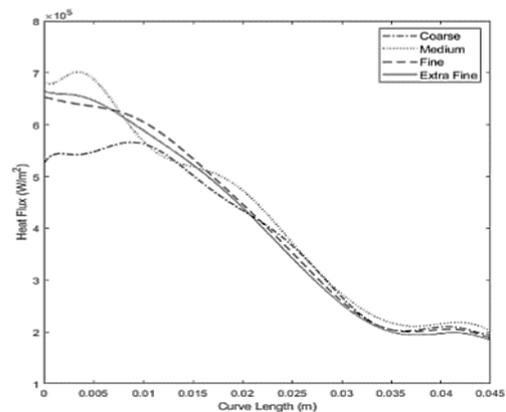

Fig. 1. Computational Grid & Boundary Conditions.

5.2 Grid Independent Study

To ensure the absence of grid dependent errors in the solution, it is essential to undergo series of simulations using multiple levels of grids. So the grid independent studies are carried out for different cases of present interest. A sample study conducted for the reference case of flow over a blunt cone model is presented here. Four levels of grids are employed, viz. coarse, medium, fine and extra-fine. \change These grid levels differ in terms of the number of nodes along the radial and angular directions of the domain as well as the $Y+$. Simulations are carried out using all four grid levels, and the numerical results obtained are presented here to prove the grid independence. Figure 2 shows the heat flux variation along the curve length for each of these grids. A significant difference is observed in the case of coarse and medium grid, however, there is negligible difference between the fine and extra fine grid. This is in accordance with the fact that the coarse and medium grid does not fulfil the criterion of $Y+<1$ required for $k-\omega$ SST model.

Fig. 2. Grid Independent Study.

5.3 Solution Validation

Computational framework of present study is initially validated by considering the no-injection case. The reference condition of 60^0 blunt cone model in a hypersonic stream is taken for this validation study. The key flow features of this case include a standing bow shock ahead of the blunt body and a high temperature, variable entropy layer behind it. The shock-stand off distance is validated with that of emperical correlations given by Billig

(1967). The shock standoff distance for the present study (34.7mm) shows high similarity with that calculated using billig correlation(34.9mm). Further to ascertain the prediction capability of the present numerical framework, the computationally obtained surface pressure distribution is compared with the analytical prediction of modified Newtonian theory proposed by Lees and Lester (1955). It is noticeable from Fig.4 that the present study's numerical solution is in close concord with the modified newtonian theory. Since the previously mentioned empirical correlations have been validated in the past, both experimentally and numerically, the authors are of the opinion that the present numerical study is accurate enough to capture the no-injection flowfield.
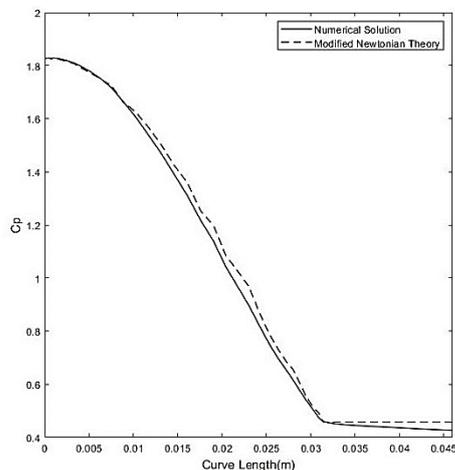

Fig. 3. Residuals history.

Fig. 4. Comparison of Pressure coefficient between Modified Newtonian law and the numerical solution.

Since the primary focus of the present study is the exploration of drag reduction through stagnation point injection, the validation of injection boundary condition opted for the current simulations is absolutely necessary. For this purpose, a pilot study

is carried out by considering the experimental conditions of Venukumar and Reddy (2007). In the original experimental work, authors investigated the case of gas injection from the orifice present at the stagnation point of a blunt cone model. The freestream employed for this study had a Mach number of 8.0. The schlieren visualization captured from the test section is used here to compare with numerically obtained flow structure. Figure 5 shows this comparison. It is evident from the Fig.5 that the shock structures for both the cases are very similar. The flow structure consists of a detached shock wave, a recompression wave, a recirculation region and a Mach disk. All these features are well captured in the numerical schlieren as well. The numerical simulation recorded a drag coefficient of 0.593 which is very close to the experimental measured value of 0.64. This promising similarities of flowfields gave the confidence to apply the same numerical strategy for subsequent parametric studies.
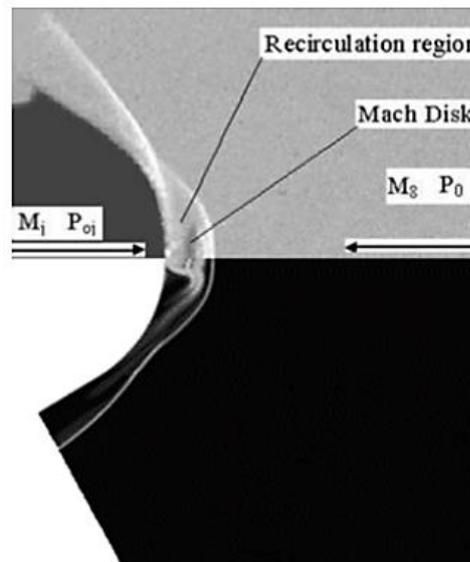

Fig .5. Flowfield comparison between numerical solution (Bottom) and Experimental solution (Top) Courtesy: Venukumar *et al*.

To further bolster the correctness of the solution, the surface Stanton number distribution obtained by simulating Mach 5.75 flowfield over the same blunt body is compared with experimental data reported by Sahoo *et al.* (2005). This additional simulation is carried out because for the Mach 8 case, experimental heat flux measurements were not available to compare with the numerical solution. It can be seen from Fig.6 that the solver prediction of Stanton number is in close agreement with experimental data, thus it validates the accuracy and correctness of solver settings employed for the present study in predicting the dissipation aspects of the flowfield.
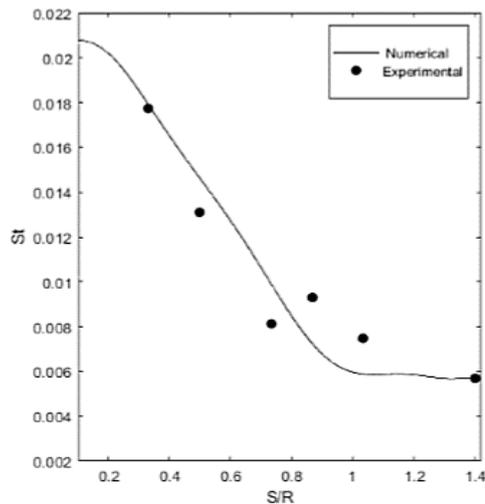
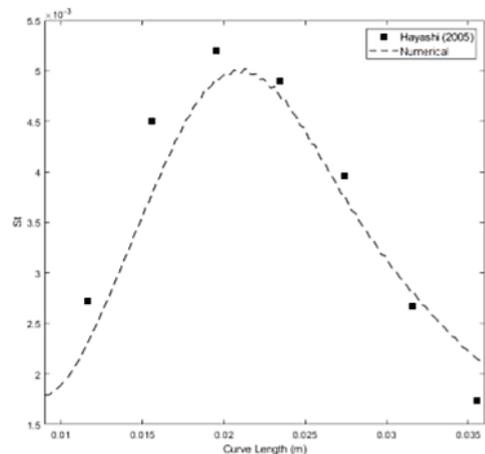**Fig. 6. Stanton number variation comparison for no injection.**

Fig. 7. Stanton number variation comparison for jet injection.

To ascertain the prediction accuracy of numerical setup employed for the injection simulation, the experimental study conducted by Hayashi *et al.* (2005) is repeated numerically. This study considered Mach 3.75 flow over a hemispherical model of 50 mm diameter. Out of the different injection pressure ratios used in the original experimental study, the case of P_{0j} / P_{01} =0.4 is taken for this validation study. The solver settings are kept same as that employed for the previously mentioned stagnation point injection simulation along with suitable boundary conditions to replicate Hayashi's experimental condition. The predicted Stanton number distribution on the hemispherical blunt model is plotted along with experimental measurements in Fig.7. An encouraging agreement between the numerical and experimental Stanton number distribution is clearly noticeable in Fig.7 and this validates the numerical frame work of present study again.

6. RESULTS & DISCUSSION

The validated numerical framework is used to explore the potential of the drag reduction techniques discussed in the above sections and evaluate the reduction in drag and surface heat flux under various parametric conditions. Finley (1966) studied the dependence of critical pressure ratio (P_{crit}) on relative body size D_r and fineness ratio λ . As evaluated by Finley, the critical pressure ratio (P_{crit}) for the present model with D_r =35 and λ =1, is found to be 6.5. For any injection pressure ratio below P_{crit} the flow is unsteady and hence irrelevant for the present study. The successful implementation of Counterflow jet requires separation of the oncoming freestream flow to a point in the rear portion of the stagnation region at reattachment. The present study focuses only on sonic injection that ensures short penetration mode of injection. The SPM flow pattern could be identical to that of short spike with aerodisk. Parametric studies are carried out by varying the pressure ratio. The pressure ratio of PR=52.3 is expected to create flow reattachment slightly downstream of the shoulder, therefore, PR=52.3 is taken as the limiting case for this study. Therefore, the injection pressure ratio is varied from 8.25 to 52.3. Authors are of the opinion that a further increase in PR may not bring about any significant reduction of wave drag and heat flux. Additionally, drag and heat flux variation through passive technique, solid spike, is also investigated. Parametric variations considered for spike cases are limited as the objective is not optimization of the spike but obtaining equivalence for various spike cases.

Effect of injection pressure ratio The surface pressure distributions obtained with different injection pressure ratios are analyzed to examine the effect of injection pressure ratio on shock layer recasting and the drag reduction. The lesser the stagnation region pressure, the lesser would be the overall drag. It can be seen from the Fig.8 that increase in injection pressure ratio reduces surface pressure at the stagnation region. However, surface pressure peaks are observed downstream of the stagnation point, which are to be attributed to the reattachment of shock layer flow to the body surface. Beyond the reattachment point surface pressure reduces, mainly due to boundary layer thickening and expansion of the flow. The observed variations in surface pressure distributions are to be analyzed on the light of shock layer alterations. Therefore, the Mach contours obtained with different injection pressure ratios are compared in Fig.9. Higher injection pressure ratio ensures higher amount of mass injected into the shock layer, resulting in a better upstream push of shock layer. The additional mass injected to the shock layer from the injection port bulges the shock layer as observed in the contours of injection cases. This in turn leads to re-casting of the bow shock into nearly oblique shock.
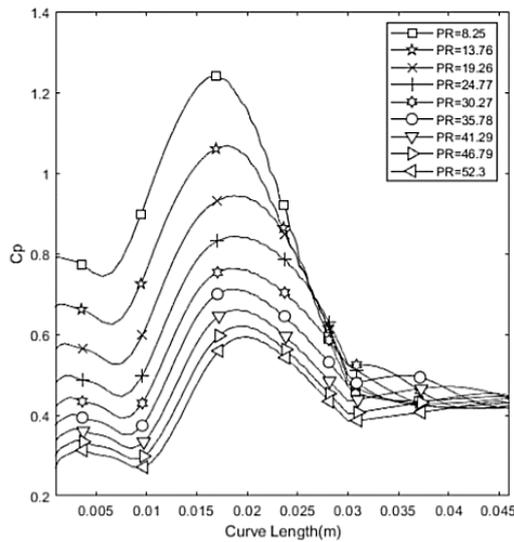
Fig. 8. Plot of C_p vs Curve length.

Further, stagnation point injection results in creation of a recirculation region bounded by the outer edge of the supersonic jet and the surface of the blunt body. The size of the recirculation region is noted to be depending on the reach of injected flow into the freestream. The Mach disk separates the injected stream and the oncoming freestream. To understand the shock stand off distance and Mach disk location, the Mach number variation along the stagnation line is captured and the same is compared with that of different injection cases in Fig. 10. There are many important aspects to note from Fig. 10, the foremost one is the expansion of injected jet from sonic velocity to supersonic speed outside the injection port. For instance, the injected jet of PR=52.3 case expanding from sonic condition to a maximum jet Mach number of 6.1. Moreover, the jet having higher speed penetrates more into the shock layer and pushes it far upstream. The Mach disk location is a clear indicator of the jet's potential in recasting the shock structure. In the Mach distribution presented in Fig.10, the Mach number suddenly drops from its freestream value to a subsonic value at a specific x-location, this is because of the deceleration of flow across the bow shock front. So this Mach-drop location can be effectively employed to calculate the shock stand-off distance at each injection case. Downstream of this shock location the Mach number remains same for a considerable x-distance, followed by a sharp rise. However, this second Mach variation should not be misinterpreted as a physical change in Mach number of the flow as in case of Mach variation across the shock.

In fact, there is no physical mechanism to have such sharp jump in Mach number. Instead the left side of this jump location indicates the decelerated freestream Mach number, whereas the right side represents the Mach number of accelerated jet. Hence this jump location is exactly the location of

Mach disk that separates two streams. The locations of Mach disk and shock front for various injection conditions can be best understood from the Fig. 9. Further, it is clear from Fig.9 that, as the injection pressure increases, the shock reattachment location shifts from the frontal portion of the blunt body to its shoulder region.

Table 2 Percentage Drag Reduction for different Injection pressure ratios

$P0j$	PR	C_d	Reduction %
No Jet	-	0.844	-
1.5	8.2580	0.7429	11.98
2.5	13.7634	0.6803	19.40
3.5	19.2688	0.6323	25.08
4.5	24.7741	0.5938	29.64
5.5	30.2795	0.5604	33.60
6.5	35.7849	0.5318	36.98
7.5	41.29	0.5013	40.60
8.5	46.7956	0.4699	44.32
9.5	52.3010	0.444	47.39

Having understood the flow structure and surface pressure variation under different injection conditions, it is vital to analyze their impact on overall drag and heat flux for the blunt body. The drag coefficient and percentage drag reduction for different injection pressure ratios are tabulated in Table 2. The drag coefficient is noted to be reducing from 0.844 of reference case (no injection) to 0.444 when the injection pressure ratio is 52.3.

It is observed that with the initial increase in injection pressure the reattachment point shifts downstream and the stagnation region pressure drops considerably. However, beyond a certain pressure ratio (PR $\approx$ 30) the reattachment location mildly shifts forward as shown in Fig. 11, while maintaining the same trend of stagnation region pressure reduction. This is the reason for the change in the rate of drag reduction with increase in injection pressure ratio. At lower injection pressure ratios counteracting momentums of freestream flow and injected stream get balanced close to the body. The Mach disk location is a quantitative representation of the location of momentum balance. As the injection pressure increases, the momentum of the injected stream also increases and helps the injected fluid to penetrate more into the shock layer. It can also be noted that with increased injection pressure ratio, the spread of the injected stream also enlarges. With the widening of the jet cone angle, the axial momentum of the jet declines and radial momentum increases slightly. With the reduced axial momentum of the injected jet, the upcoming supersonic jet can confine and force the shear layer to attach on the frontal
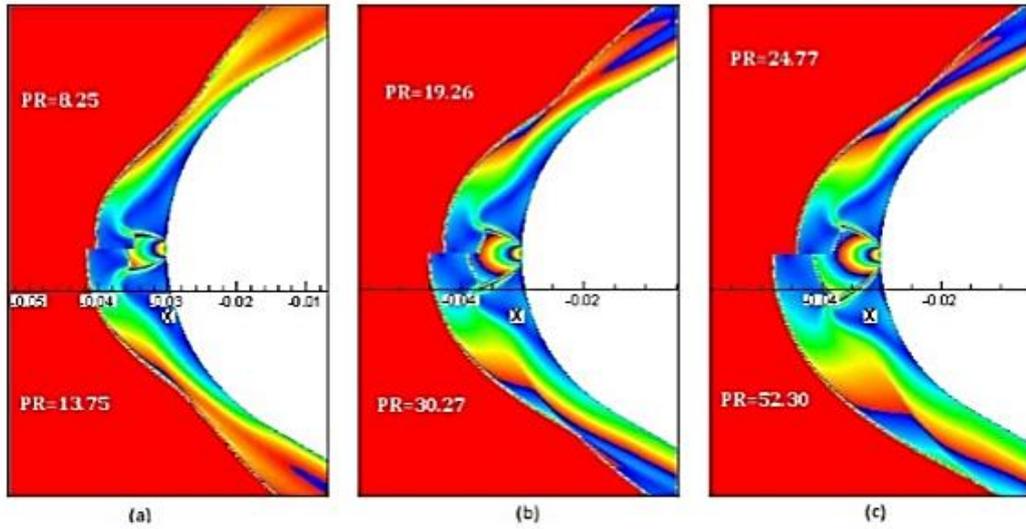
Fig. 9. Comparison of Mach Contours for (a) PR=8.25 and PR=13.75 , (b) PR=19.26 and PR=30.27, (c) PR=24.77 and PR=52.30.
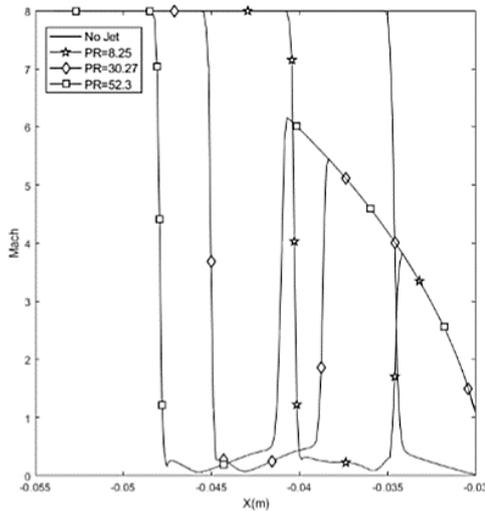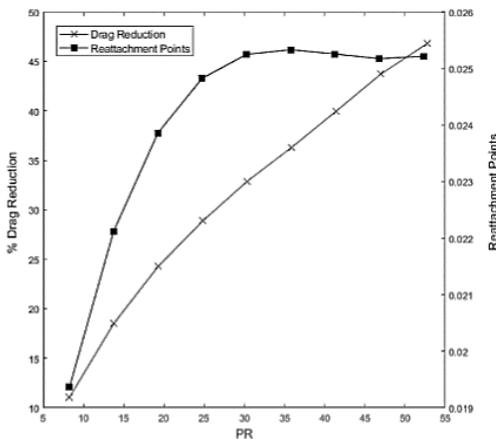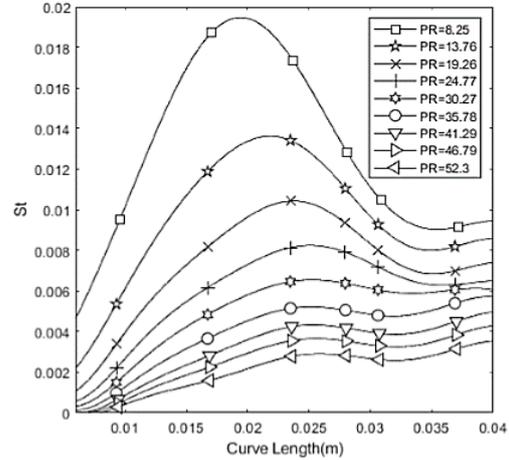

Fig. 10. Plot of Mach vs X.

Fig. 12. Plot of Stanton number vs Curve length for different Pressure Ratios.

region of the blunt body much effectively. This may be the reason for the forward movement of the reattachment location beyond PR=30. Thus, it can be inferred that use of very high injection pressure ratio may not fetch considerable improvement in drag reduction. Further projection of the drag curve and the drag-reduction trend given in Fig.11 , is expected to show flattened trend lines at very high values of injection pressure ratios.

It is equally important to analyze surface heat flux along with drag reduction, since the design of thermal protection system is a key aspect for the successful realization of hypersonic vehicles. Hence, the surface heat flux distributions obtained with various injection pressure ratios are inspected in terms of Stanton number and are plotted in Fig.12. Similar to that in the case of surface pressure, the stagnation region of the blunt body experiences very low heat flux in the presence of injection. This

Fig. 11. Plot of percentage drag reduction and shock reattachment point vs Pressure Ratio.

evidences the cooling effect offered by the injected flow. It is to be noted here that the injection temperature was 300K, whereas the freestream static temperature was 172.4 K. In the case of no-injection (reference case), the Stanton number at the stagnation region is approximately 0.033. On the other hand all the injection cases recorded Stanton number values lower than this value at the stagnation region. The cooling effect noticed at the stagnation region is to be attributed to the cold recirculation region formed ahead of the blunt body while the injection is active.

On visualizing the flowfield through Mach contours (Fig.9), it can be noticed that the recirculation region created due to stagnation point injection plays an important role. When the injection is active the jet flow passes through the Mach disk and meets the freestream flow thereby constituting a counter-directional secondary flow which acts as a heat blanket, separating the freestream flow from the body. With the increase in injection pressure ratio, the injected air gets the chance to expand to higher Mach numbers outside the injection nozzle, as evident in Fig.10 . Since the injection temperature is maintained as same for all the injection pressure ratios, the highly expanded jet will have lesser static temperature compared to less expanded jet. This indicated that with the increase in injection pressure, the average temperature of recirculating cold blanket ahead of the blunt body will reduce. Therefore, the gradient of temperature near the wall reduces and thereby results in decay of surface heat flux. This observation implies that heat flux reduction associated with increase in injection pressure may also depend on the ability of the injection system to maintain constant injection temperature for a range of injection pressure.

The validated numerical framework is also employed to simulate the passive technique of using a solid spike to ascertain the change in drag and heat flux, which further is compared with different injection pressure ratio cases of Counterflow jet. The solid spike protruding from the stagnation point of the blunt body deflects a considerable amount of flow thus preventing the entire ram of the freestream flow which otherwise it would have to endure. To comprehend the effect of spikes on the blunt body, it is necessary to examine the angle of lip shock (spike leading edge shock) which is measured from the horizontal and causes most of the deflection of upstream flow, the shear layer encompassing the region of recirculation and the location of the reattachment of the flow. The shape of the spike influences the flow deflection angle whereas the spike length and diameter determine the amount of flow that is deflected.

The study involved investigation of two different types of spike, blunt and pointed, each with L/D=0.5 and L/D=1. The investigation suggests that the more the downstream shift of the flow reattachment point, as in the case of L/D=1 than L/D=0.5, the lesser would be the stagnation region pressure which would

result in reduced drag. Moreover, as the length of the spike is increased, the angle of inclination of the separation zone decreases causing the size of the recirculation region to increase which in turn would decrease the pressure and density behind the shock within the recirculation region. Therefore, the short spike (L/D=0.5) is less effective in reducing drag than long spike (L/D=1). Hence, it can be concurred that by increasing the L/D ratio, more drag reduction is achieved irrespective of the shape of the spike. Similar observations have been reported by Sahoo *et al.* (2016).

To discern the superiority among the two types of spikes investigated, blunt and pointed spike of same L/D ratio are compared. When using a blunt spike, a detached bow shock is formed at the leading edge of the spike as opposed to an attached conical shock in the case of pointed spike. The detached bow shock significantly alters the flowfield downstream. A variable entropy layer is formed over the developing boundary layer on the spike surface. At any location, where the height of entropy layer exceeds that of the boundary layer, the boundary layer would possess a greater stability against separation (John and Kulkarni 2014). On the contrary, if the boundary layer completely swallows the entropy layer, separation of flow would occur due to the reduction in density within the boundary layer.

Table 3 Percentage Drag Reduction for different Spikes

Spike	L/D	C_d	% Reduction
Pointed	0.5	0.8025	4.91
Pointed	1	0.7325	13.21
Blunt	0.5	0.695	17.65
Blunt	1	0.5826	30.97

The Mach contours comparison presented in Fig.13 clearly indicates that the separation point of blunt spike is ahead of pointed spike. Since the radius of bluntness is very less for the blunt spike, the entropy layer created in this case is getting completely swallowed by the boundary layer leading to early separation. The drag coefficient (C_d) values of spike cases are tabulated in Table 3.

It can be seen from Table3 that blunt spike is superior than the pointed spike, since it exhibited more drag reduction. Primarily , the upstream shift of the recirculation zone on the surface of the spike and the downstream shift of the reattachment point, as evident from Fig.13 , are responsible for the better drag reduction attained by the blunt spike. The downstream shift of the reattachment point location causes peak pressure at the aft of the blunt body, therefore offering a relatively higher drag reduction as opposed to the pointed spike. Furthermore, another reason for the observed lower drag coefficient values for blunt spike can be attributed to
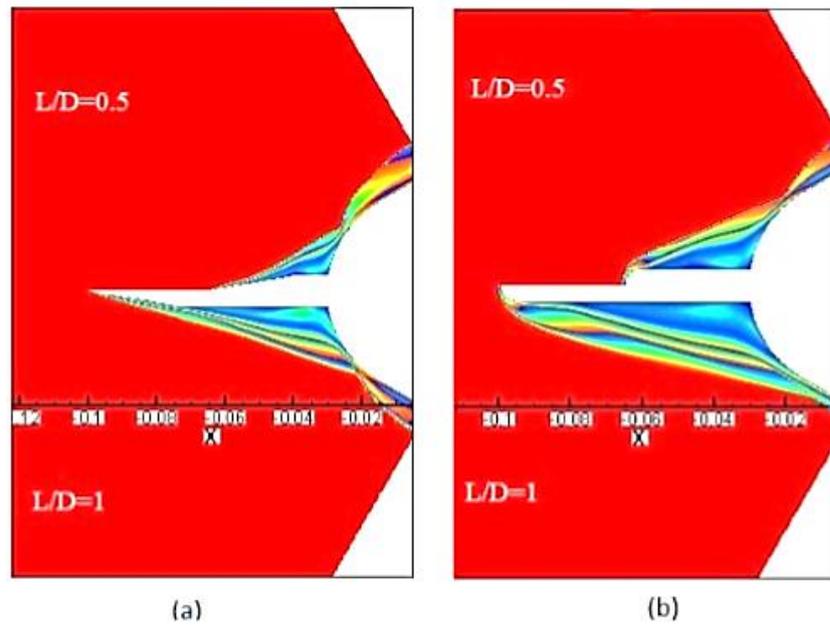
Fig. 13. Mach contours comparison for (a) Pointed spike L/D=0.5 & 1 (b) Blunt spike L/D=0.5 & 1.

the curved shape of the spike's leading edge shock, due to which the oncoming flow suffers higher deflection away from the blunt body's stagnation region and hence results in lesser amount of oncoming flow plunging the blunt body.

The Stanton number variations obtained with different spike cases are compared in Fig.14 to understand the heat flux reduction potential of the solid spike. Stanton number distributions corresponding to different spike cases is evidence, that the stagnation region heat flux reduces in the presence of forward facing solid spike. This observed reduction in stagnation region heat flux can be attributed to the existence of recirculation region ahead of the blunt body. However, it is to be noted that this reduction in heat flux on the surface of the blunt body is at expense of spike tip overheating. Therefore, frequent replacement of spike may be required.

6.1 Equivalence Cases

On identifying the potential of both techniques, the equivalence of these two techniques is explored. In this study, the passive technique of solid spike is taken as reference, and the active technique of counterflow injection is adjusted with different injection pressure ratios to get the same drag. The drag coefficients for both the spike types, blunt and pointed for L/D=0.5 & 1 were obtained. Multiple iterations were carried with different injection pressure ratios, to discern equivalent active drag reduction cases which results in drag similar to the passive cases. Several equivalence cases were identified on the basis of equal drag. The equivalence cases are tabulated in Table 4.
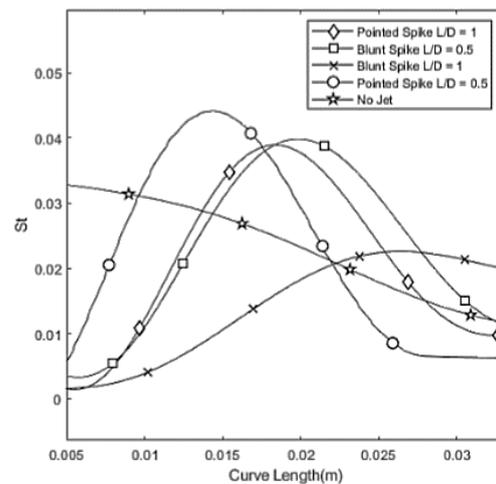

Fig. 14. Plot of Stanton number vs Curve length for different spikes.

Table 4 Equivalence Cases

Case	Method Type	C_d
1	Pointed Spike (L/D=1) Counterflow Jet (PR=8.25)	0.7325 0.7429
2	Blunt Spike (L/D=0.5) Counterflow Jet (PR=13.76)	0.695 0.6803
3	Blunt Spike (L/D=1) Counterflow Jet (PR=24.77)	0.5826 0.5938

The peak pressure coefficient and peak Stanton number are depicted using a spider chart as shown in Fig. 15 . It can be observed that in the equivalence cases obtained, although the solid spike gives almost same drag, the peak pressure in the case of spike is always greater than the corresponding equivalent jet pressure case, as given in Table 5(a). Thus, the structural integrity will be more in the case of counterflow jet. Moreover, as shown in Table 5(b), for each of the equivalence cases, heat flux is lower for counterflow jet than that of the corresponding spike case resulting in better thermal protection.

Table 5 Equivalence case comparison of peak Pressure and peak Heat Flux

Peak Pressure (*Pa*)		
Case	Spike	CDR
1	17598.4	12392.5
2	14833.7	10695.3
3	8081.77	8486.36

(a)

Peak Heat Flux (*W/m²*)		
Case	Spike	CDR
1	818379	383908
2	874677	282004
3	461860	221890

(b)

6.2 Effectiveness of Drag Reduction Techniques

Another important aspect of comparison is the effectiveness (ϵ) of drag reduction technique. This term is defined as the amount of power saved due to the drag reduction to the amount of power spent to achieve the drag reduction. The spike, being a passive drag reduction technique, doesn't require any input energy to function. Thus, theoretically the effectiveness of physical spike is infinite. On the other hand, the active technique, counterflow injection requires input energy to inject the fluid into the shock layer. Hence it is meaningful to define the effectiveness of counter flow injection technique as:

$$\epsilon = \frac{(F_0 - F)V_\infty}{(P_{0j} - P_{02})\dot{Q}}$$

Where, F_0 is the reference drag, F is the computed value of drag for a given injection pressure, V_∞ is the flight speed, $\dot{Q}$ represents the volume flow rate and $P_{0j} - P_{02}$ is the total pressure difference between the shock layer and nozzle exit. The rate of energy saving due to drag reduction, rate energy consumption and effectiveness of injection technique are plotted against pressure ratio in Fig. 16. It can be noted that the amount of energy saved increases with pressure ratio, while the energy required for injection also shows the same trend. Hence the effectiveness of injection technique decreases with increase in pressure ratio. However, on considering the amount energy saved at higher pressure ratios, it is recommended to use higher injection pressures even though the effectiveness of those cases are comparatively low.

7. CONCLUSION

Simulations are carried for a 60^0 apex angle blunt cone having 70 mm base diameter and bluntness ratio of 0.857 in a freestream of Mach 8. Two different drag reduction techniques, active (solid spike) and passive (counterflow injection) are evaluated to identify their potential to reduce drag and heat flux. The main focus of the study however is to discern equivalence cases between these two methods. For the counterflow injection technique, the injection pressure ratio is varied from 8.25 to 52.3. It is observed that on increasing the injection pressure ratio, the drag reduces but only up to a certain pressure ratio. Beyond this pressure ratio, the drag reduction becomes insignificant. A maximum of 47\% drag reduction from no jet case is achieved for PR=52.3. Moreover, heat flux also decreases considerably with increasing injection pressure ratio thus offering easier thermal protection. In the case of spikes, it is determined that irrespective of the spike shape, the long spike of L/D=1 provides better drag reduction as opposed to the short spike of L/D=0.5. On increasing L/D ratio from 0.5 to 1, an improvement of almost 9\% and 16\% is observed for pointed and blunt spike respectively. Furthermore, higher drag reduction is achieved when using blunt spike in place of pointed spike. Blunt spike with L/D=0.5 enhanced drag reduction by almost 18\% as opposed to same L/D pointed spike which provided only 5\% drag reduction. For L/D=1 case, blunt spike yet again offered 31\% drag reduction as opposed to 13\% with pointed spike of same L/D ratio. Based on the investigations, equivalence cases are evaluated.

For a pointed spike of L/D=1, a counterflow injection with PR=8.25 delivers almost the same drag. Interestingly, for this particular equivalence case, the peak pressure and peak heat flux values obtained for Counterflow jet are found to be almost 30\% and 53\% lower respectively, than the solid spike case. A Similar trend is observed for the equivalence cases of blunt spike of L/D=1 and L/D=0.5 with a counterflow injection of PR=24.77 and PR=13.76 respectively. This indicates that even though the spike can provide same overall drag as counterflow injection, the latter is always a better option considering the structural integrity and thermal protection.
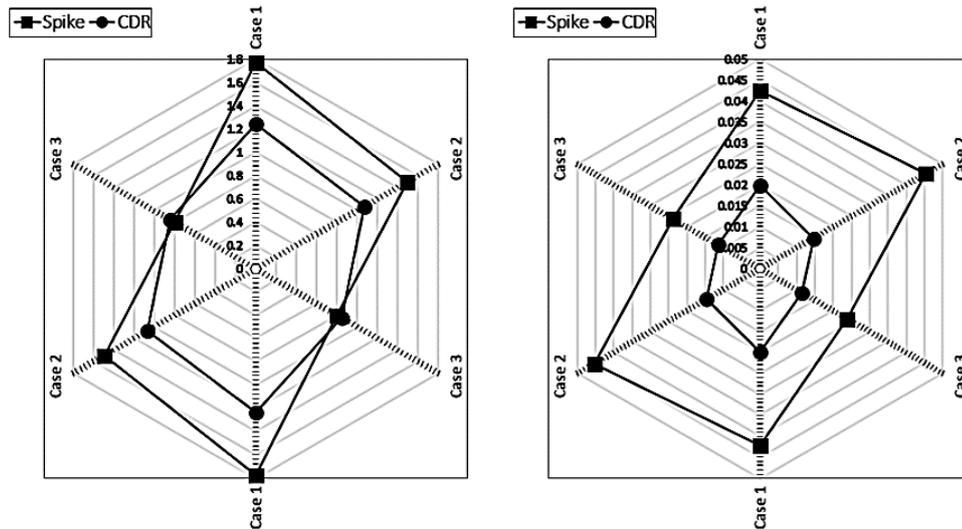
Fig. 15. Spider Chart depicting the (a) Peak *Cp* Variation and (b) Peak Stanton number Variation for the equivalence cases.
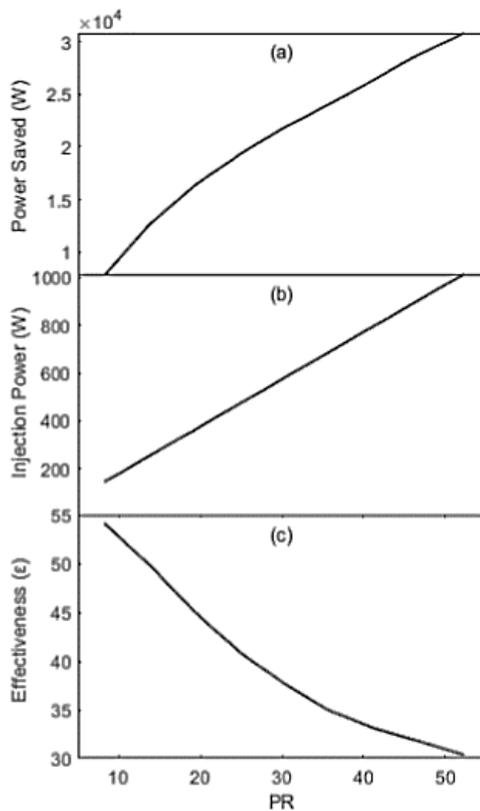

Fig. 16. Plot of Power Saved(a), Injection Power(b) and Effectivness(c) vs PR.

REFERENCES

Allen, H. J., & Eggers Jr, A. J. (1958). A study of the motion and aerodynamic heating of ballistic missiles entering the earth's atmosphere at high supersonic speeds, NACA-TR-1381, Forty-Fourth Annual Report of the NACA, 1125-1140.

Anderson, J. D. (2006). Hypersonic and High Temperature Gas Dynamics, American Institute of Aeronautics and Astronautics. Inc.: Reston, VA, USA, 395-406.

ANSYS 18.0. ANSYS Inc. Version 18, Canonsburg, PA, USA.

Billig, F. S. (1967). Shock-wave shapes around spherical-and cylindrical-nosed bodies. *Journal of Spacecraft and Rockets* 4(6), 822–823.

Bogdonoff, S. M. (1959). Preliminary investigations of spiked bodies at hypersonic speeds. *Journal of the Aerospace Sciences* 26(2), 65–74.

Crawford, D. (1959). Investigations of the flow over a spiked-nose hemispherecylinder. *NASA TN D-118*.

Deng, F., F. Xie, N. Qin, W. Huang, L. Wang and H. Chu (2018). Drag reduction investigation for hypersonic lifting-body vehicles with aerospike and long penetration mode counterflowing jet. *Aerospace Science and Technology* 76, 361–373.

Feszty, D., K. J. Badcock and B. E. Richards (2004). Driving mechanisms of high-speed unsteady spiked body flows, part i: pulsation mode. *AIAA journal* 42(1), 95–106.

Finley, P. (1966). The flow of a jet from a body opposing a supersonic free stream. *Journal of Fluid Mechanics* 26(2), 337– 368.

Gerdroodbary, M. B. and S. Hosseinalipour (2010). Numerical simulation of hypersonic flow over highly blunted cones with spike. *Acta*

Astronautica 67(1-2), 180– 193.

Hayashi, K., S. Aso and Y. Tani (2005). Numerical study of thermal protection system by opposing jet. In *43rd AIAA Aerospace Sciences Meeting and Exhibit*, 188.

John, B. and V. Kulkarni (2014). Effect of leading edge bluntness on the interaction of ramp induced shock wave with laminar boundary layer at hypersonic speed. *Computers & Fluids* 96, 177 – 190.

Kalimuthu, R., R. C. Mehta and E. Rathakrishnan (2010). Drag reduction for spike attached to blunt-nosed body at mach 6. *Journal of Spacecraft and Rockets* 47(1), 219–222.

Kalimuthu, R., R. Mehta and E. Rathakrishnan (2019). Measured aerodynamic coefficients of without and with spiked blunt body at mach 6. *Advances in aircraft and spacecraft science* 6(3), 225–238.

Kulkarni, V. and K. Reddy (2008). Enhancement in counterflow drag reduction by supersonic jet in high enthalpy flows. *Physics of Fluids* 20(1), 016103.

Lees, L. (1955). Hypersonic flow. *Fifth International Aeronautical Conference, Los Angeles, 1955, Inst. of Aeronautical Sciences, New York*, pp 241–276.

Li, S. B., T. T. Zhang, C. Ou, W. Huang and J. Chen (2020). Mechanism study on drag reduction and thermal protection for the porous opposing jet in hypersonic flow. *Aerospace Science and Technology*, 105933.

Mehta, R. (2013). Numerical heat transfer study around a spiked blunt-nose body at mach 6. *Heat and Mass Transfer* 49(4), 485–496.

Menter, F. R. (1994). Two-equation eddyviscosity turbulence models for engineering applications. *AIAA journal* 32(8), 1598–1605.

Panaras, A. G. and D. Drikakis (2009). Highspeed unsteady flows around spiked-blunt bodies. *Journal of Fluid Mechanics* 632, 69–96.

Sahoo, D., S. Das, P. Kumar and J. Prasad (2016). Effect of spike on steady and unsteady flow over a blunt body at supersonic speed. *Acta Astronautica* 128, 521– 533.

Sahoo, N., V. Kulkarni, S. Saravanan, G. Jagadeesh and K. Reddy (2005). Film cooling effectiveness on a large angle blunt cone flying at hypersonic speed. *Physics of Fluids* 17(3), 036102.

Venukumar, B. and K. Reddy (2007). Experimental investigation of drag reduction by forward facing high speed gas jet for a large angle blunt cone at mach 8. *Sadhana* 32(1-2), 123–131.

Venukumar, B., G. Jagadeesh and K. Reddy (2006). Counterflow drag reduction by supersonic jet for a blunt body in hypersonic flow. *Physics of Fluids* 18(11), 118104.

Warren, C. H. E. (1960). An experimental investigation of the effect of ejecting a coolant gas at the nose of a bluff body. *Journal of Fluid Mechanics* 8(3), 400–417.

Wood, C. (1962). Hypersonic flow over spiked cones. *Journal of Fluid Mechanics* 12(4), 614–624.

Yamauchi, M., K. Fujii and F. Higashino (1995). Numerical investigation of supersonic flows around a spiked blunt body. *Journal of Spacecraft and Rockets* 32(1), 32–42.

Yisheng, R. (2013). Drag reduction research in supersonic flow with opposing jet. *Acta Astronautica* 91, 1–7.

Zhang, R.-r., W. Huang, L.-q. Li, L. Yan and R. Moradi (2018). Drag and heat flux reduction induced by the pulsed counterflowing jet with different periods on a blunt body in supersonic flows. *International Journal of Heat and Mass Transfer* 127, 503–512.

Zhou, C., W. Ji, X. Zhang and L. J. Deng (2013). Numerical investigation on counter-flow jet drag reduction of a spherical body. *Engineering Mechanics* 30(1), 441–447.